Journal of Materials Chemistry C

ROYAL SOCIETY OF CHEMISTRY

PAPER

View Article Online
View Journal | View Issue

Cite this: J. Mater. Chem. C, 2022, 10, 16706

Impact of crystal growth diversity on magneto-photoluminescence and circular dichroism in chiral lead halide perovskites†

Ruiheng Pan,[abc] Jiaji Hu,[ab] Sheng Tao,[ab] Lixuan Kan,[ab] Haomiao Yu [ab] and Kai Wang *[ab]

Received 9th September 2022,
Accepted 20th October 2022

DOI: 10.1039/d2tc03810b

rsc.li/materials-c

Chiral-induced magneto-photoluminescence (magneto-PL) is a newly raised magneto-optical phenomenon, where photoluminescence intensity can be effectively manipulated by magnetic fields and material helicity. By far, little is known regarding the impact of crystallographic orientations on chiral-induced magneto-PL and circular dichroism (CD) for solution-made polycrystalline chiral lead halide perovskites (LHPs). By tuning weight percentages (wt%) rationally for precursor solutions in the work, we found that large magneto-PL (−13.2%) with strong tunability *via* polarized photoexcitation is highly decided by the crystallographic orientations for the chiral LHPs. The large effect stems from the effectiveness of magnetic field modulation to excitonic fine structures. We also found that diploe-allowed excitonic transitions and the CD characters could be dramatically influenced by crystallinities. Thus, a full understanding of its growth mode and optical properties is of paramount importance for achieving large magneto-PL with strong tunability. The work opens a new avenue for chiroptical applications.

1. Introduction

Organic–inorganic hybrid perovskites (OIHPs) have gained unprecedented attention since their first discoveries in applications of solar cells and light emitting diodes (LEDs).[1] This is mainly due to their high color purities, large photo-luminescent quantum yields (PLQYs), and tunable emissive wavelengths *via* low temperature solution means.[2–5] In all sorts of OIHPs, quasi-two dimensional (quasi-2D) hybrid perovskites are the most desirable candidates for light emissions.[6–8] Organic interlayers on one hand can form shields for oxygen and moisture permeations.[9] Moreover, the quasi-2D hybrid perovskites are endowed with quantum-well confined electronic structures, giving rise to the dielectric confinement for photo- and electrically generated excitons. In order to further enrich their novel functionalities in light emitting and display technologies, to incorporate chiral organic ligands into inorganic octahedral crystalline frameworks forming chiral perovskites can broaden their applications for circularly polarized light (CPL) emissions and detections.[10–12] As a matter of fact, they can be potentially applied for spin transport, nonlinear optics, ferroelectricity and ferroelastic switches.[13–17] Recently, a large and tunable magneto-optical effect such as magneto-photoluminescence (magneto-PL) was demonstrated.[18–20] Because of the innate chirality, the chiral perovskites contain some unique spin-related chiroptical properties. Their natural optical activities (NOAs) such as the circular dichroism (CD) and CPL are effectively controlled by the so-called chiral-induced spin–orbit coupling (CISOC).[21] In this respect, only one spin-channel is dominant, either left or right polarized photo-absorption and emission. Such a behavior refers to chirality-induced spin selectivity (CISS).[22] It is also applicable for the charge-spin conversion in electronic transport.[23]

In order to achieve a decent CD, rational designs for crystallinities and phase arrangements may be required for solution-processable 2D chiral perovskites.[24–27] Analogously, these have been always concerned with conventionally achiral quasi-2D perovskites for high performance LEDs.[28–30] As we know, the crystallinities and phases are decisive for electronic structures, like dimensions, energy gaps and charge transport routes.[31] Highly regular and well-defined phases for alternating organic–inorganic configurations can guarantee periodic quantum well structures, which gives rise to strong quantum confinement for excitons.[32] It is also a merit for luminescence efficiency and color purity in conventional 2D perovskites. In addition, an assembly of multiple phases with different number of inorganic

[a] Key Laboratory of Luminescence and Optical Information, Ministry of Education, School of Physical Science and Engineering, Beijing Jiaotong University, Beijing, 100044, China. E-mail: kaiwang@bjtu.edu.cn
[b] Institute of Optoelectronics Technology, Beijing Jiaotong University, Beijing, 100044, China
[c] School of Science, Chongqing University of Posts and Telecommunications, Chongqing, 400065, China

† Electronic supplementary information (ESI) available. See DOI: https://doi.org/10.1039/d2tc03810b

frameworks may successfully yield the funnel-based charge and energy transfer behaviors.[31,33,34] Yet, it remains a question mark for an understanding of crystallinity and phase arrangement on chiral perovskites as they also involve magnetic responses; by far, relevant studies for their impact on the chiral-induced magneto-PL and CD behaviors are deficient.

In the article, we attempt to study the impact of crystallographic orientations on the chiral-induced magneto-PL and the CD characters for chiral lead halide perovskites (LHPs). Some different crystallinities can be realized by tuning precursor solution weight percentages (wt%). A large magneto-PL effect with strong tunability can be measured for a specific sample, while it requires an effective field manipulation for excitonic fine structures. The change of the crystallographic property may influence dipole-allowed exciton transitions for the chiral LHPs. The work highlights an overriding role to correlate material properties with their chiroptical characteristics.

2. Experimental section

2.1 Material synthesis

In the work, we chose the prototypical *R*-methylbenzylamine lead iodide ($(R\text{-MBA})_2PbI_4$) and *S*-methylbenzylamine lead iodide ($(S\text{-MBA})_2PbI_4$) as the left- and right-handed chiral LHPs, respectively. All chemicals were commercially available products. During the chemical syntheses, 200 mg lead oxide (PbO), 200 μl *R*- or *S*-MBA, and 6 ml aqueous hydriodic acid (HI) solution were mixed in a glass vial. Some yellow precipitates are formed immediately. Then, the vial was immediately transferred to an oil bath. The temperature of the solution was set to be 100 °C in order to dissolve the precipitates. After this, the temperature was reduced to the room temperature naturally. From the observation of the vial, an assembly of single crystalline needles could appear in the solution. All the crystals were filtrated and rinsed with toluene. Subsequently, they were completely dried in an oven for 12 hours for getting rid of the moisture.

Prior to the fabrication of polycrystalline thin films, the chiral perovskite single crystals were dissolved in an organic solvent, for instance, *N*,*N*-dimethylformamide (DMF, 99.9%). Different concentrations of solutions were prepared by weighing different amount of the crystals on a balance. In our experiment, the wt%s were distinguished by the 10 wt%, 20 wt%, 30 wt%, 40 wt% and 60 wt%. After being fully dissolved in the organic solvent, the polycrystalline thin films were fabricated using the spin coating method in an ultra-high purity nitrogen glove-box.

2.2 Material characterizations

Steady state photoluminescence (SSPL) spectra were recorded using a fluorescence spectrometer (Horiba Fluorolog-3). UV-visible photo-absorption spectra were obtained by an absorption spectrometer (Shimadzu UV-2600). Film surface crystallinities and morphologies were examined using an X-ray diffractometer (XRD) and a scanning electron microscope (SEM, GeminiSEM 500). Absorbance of left- and right-circularly polarized light by chiral perovskites were characterized using a CD spectrometer (Jasco-1500). The grazing-incidence wide-angle X-ray scattering (GIWAXS) was adopted for gaining in-depth understandings of samples' crystalline phases under the ambient condition. The X-ray wavelength was set to be 1.5405 Å. All the material characterizations were carried out at room temperature.

2.2 Magneto-PL luminescence measurements

During magneto-PL measurements, a sample was mounted on a cold finger inside an enclosed cryogenic system. The system located inbetween a pair of electromagnets with a maximum field strength of 2 Tesla. A combination of a semiconductor laser (λ = 405 nm), a linear polarizer, a quarter-wave plate, and an optical fiber-integrated fluorescence spectrometer was used for photo-excitation and collection. A variation in the peak value of the PL spectrum was recorded in a sweeping field. The calculation of the magneto-PL in percentage is $\left(\frac{\mathrm{PL}(B)}{\mathrm{PL}(0)}-1\right)\times 100\%$, where the PL($B$) and PL(0) are the PL intensities measured with and without B, respectively.

3. Results and discussion

The photographic images for the orange colored needle-like single crystals $(R\text{-MBA})_2PbI_4$ are provided in Fig. S1(a) of the (ESI†). The images of the solution-processed polycrystalline thin films due to the different wt% are displayed in Fig. S1(b) (ESI†). The distinct color strengths may be ascribed to the film thickness and surface morphology. Fig. 1(a) shows the steady state photoluminescence (SSPL) spectra at 4 K for the films with the different wt%. When the films were placed inside a helium-free cryogenic system, the photo-induced fluorescence could be observed and the spectrum could be captured through a viewing port (lower inset of Fig. 1(a)) *via* an optical fiber. Manifestly, the 20 wt% sample has the strongest SSPL intensity with the dominantly emissive wavelength at λ = 513 nm. Others, of the different wt%, exhibit reduced fluorescence intensities. The upper inset plot of Fig. 1(a) is the corresponding normalized SSPL spectra. Judging from the inset plots, there are no noticeable shifts for the spectra by tuning the wt%. In spite of the intensity, there are no changes for the lineshape and the emissive peak position of the spectra. Fig. 1(b) shows the experimental results of the magneto-PL for the $(R\text{-MBA})_2PbI_4$ polycrystalline thin films with five different wt%, such as 10, 20, 30, 40 and 60 wt%. During the measurements, the sample was continuously photoexcited by the left (σ^+) or right (σ^-) circularly polarized monochromatic laser beam (λ = 405 nm). Meanwhile, the variation in the peak value for the fluorescence at 513 nm was constantly recorded in the magnetic sweeping fields inbetween ±900 mT. As we can see from the plots, all the magneto-PL has a negative sign with different magnitudes. The signals are all symmetric with respect to the zero field and their lineshapes are identical. The 20 wt% sample produces the

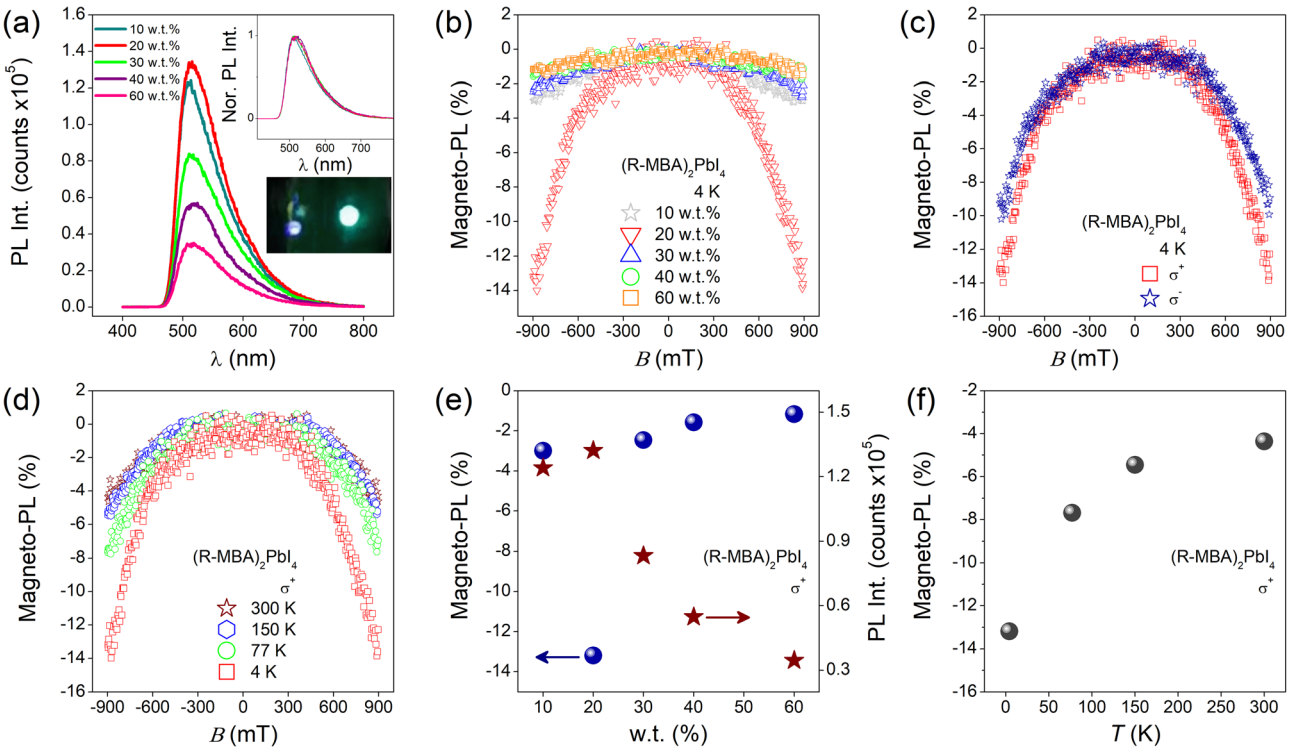

Fig. 1 (a) Experimental results of steady state photoluminescence spectra at room temperature for the (R-MBA)$_2$PbI$_4$ thin films prepared by the precursor solutions with different weight percentages (wt%), such as 10 wt%, 20 wt%, 30 wt%, 40 wt%, and 60 wt%. The upper inset plot shows the normalized spectra for the samples. The lower inset image is the photographic picture for the luminescence in the measurement. (b) The wt% dependence of the magneto-PL (%) at 4 K for (R-MBA)$_2$PbI$_4$. (c) The measurements of magneto-PL (%) due to the left and right circularly polarized photoexcitation (σ^+ and σ^-) at 4 K for (R-MBA)$_2$PbI$_4$. (d) The temperature dependence of magneto-PL (%) for (R-MBA)$_2$PbI$_4$. (e) and (f) show the extracted values for the wt% and temperature-dependent magneto-PL (%). The photoexcitation wavelength is set to be 405 nm for all the measurements.

strongest effect of approximately −13.2%. Despite this, the increase of the wt% tends to reduce the effect. Fig. 1(c) shows the magneto-PL for the left handed (R-MBA)$_2$PbI$_4$ polycrystalline thin film with the 20 wt% only at 4 K. Apparently, the (σ^+) generates relatively greater effect than the one of the (σ^-) (−9.3%). Moreover, the temperature-dependent magneto-PL for the film under the (σ^+) photoexcitation is shown in Fig. 1(d) and (e), which summarize the wt% dependence of the magneto-PL and SSPL intensity at 513 nm. The largest photoluminescence intensity corresponds to the strongest magneto-PL effect. The change in the numerical value for the magneto-PL due to the different temperatures is shown in Fig. 1(f). The decrease of the temperature from 300 K to 4 K causes the increase of the magneto-PL from −4.4% to −13.2%. The same measurements have been performed for the right handed (S-MBA)$_2$PbI$_4$ polycrystalline thin films and the experimental results are shown in Fig. S2 (ESI†). Because of the material chirality, the (σ^-) produces relatively larger effect than the one for the (σ^+). We also observed the temperature-dependent magneto-PL for the right handed (S-MBA)$_2$PbI$_4$. As we can see from the results in Fig. S3 (ESI†), it also exhibits the largest effect at 4 K.

In a view to explain the wt%-dependent magneto-PL for the chiral LHPs, we thought about the studies of material crystallographic and optical properties. First, the crystalline structures for the solution-processable (R-MBA)$_2$PbI$_4$ and (S-MBA)$_2$PbI$_4$ polycrystalline thin films with different wt% were examined *via* SEM. As we know, they are prone to the Ruddlesden–Popper (RP) type 2D perovskite crystals. Fig. 2(a)–(e) are the SEM images for the surface morphologies of the (R-MBA)$_2$PbI$_4$ thin films with the wt% of 10, 20, 30, 40 and 60, respectively. The same measurements were carried out for the counterpart (S-MBA)$_2$PbI$_4$ polycrystalline thin films. Apparently, the change in the wt% has a remarkable impact on the morphology and crystallinity. When it is increased from 10 to 60 wt%, the surface becomes rough. Some crystalline voids on top of the surface can be clearly observed for the one made of 60 wt%. The results are equally the same for the (S-MBA)$_2$PbI$_4$ polycrystalline thin films (Fig. 2(f)–(j)) fabricated under the same condition.

In order to quantify the crystallinity and crystalline phase for the chiral LHPs, we characterized them using the XRD method. Fig. 3(a) shows the out-of-plane XRD spectrum for the (R-MBA)$_2$PbI$_4$ thin film with 20 wt% under the ambient condition. Others of the different wt% are given in the supporting information (Fig. S4, ESI†). As we can see from the spectrum in Fig. 3(a), the successive diffracted bands are indexed by the (002), (004), (006), (008) and (0010) crystalline phases. The corresponding diffracted angles are at approximately 6.25°, 12.35°, 18.55°, 24.80° and 31.15°. Among these, the (002) one

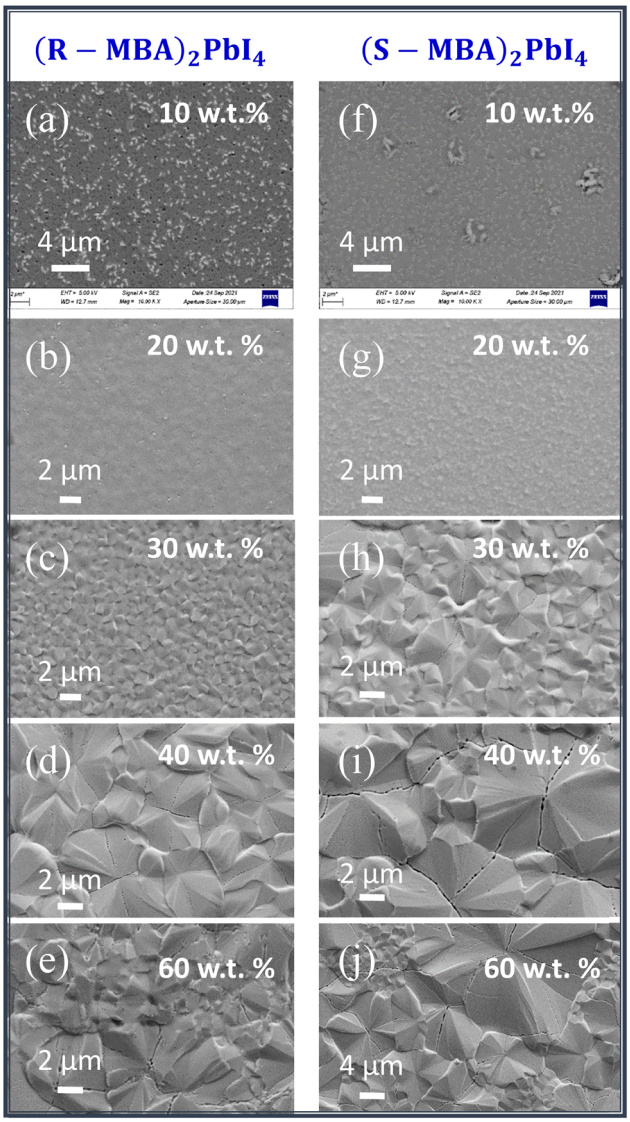

Fig. 2 SEM surface morphological images for (a–e) (R-MBA)$_2$PbI$_4$ and (f–j) (S-MBA)$_2$PbI$_4$ polycrystalline films, due to the different wt% (*i.e.*, 10 wt%, 20 wt%, 30 wt%, 40 wt% and 60 wt%).

exhibits the strongest diffracted intensity. Despite the 002l (l = 1, 2, 3, 4, 5) diffracted peaks, there are no observations for any other impure phases. In order to make a deep exploration for the spectra, we dealt all the diffracted bands with the Lorenzian fitting function. The diffracted intensities and full width at half maxima (FWHM) of the spectra have been evaluated. In the cases, the zoom-in plots that correspond to the (002) crystalline plane have been analyzed since these hold a dominant role in crystallinity. The insets (i) and (ii) of Fig. 3(a) are the two plots of the (002) diffracted band for the wt% of 10, 20 and 40 wt%. When it changes from 10 to 20 wt%, we can clearly observe a dramatic increase in intensity and the band shifts towards a smaller angle from 6.4° to 6.25°. Further increase of the wt% up to 40 wt% leads to an extensive enhancement in the intensity without a noticeable band shift. The insets (iii) and (iv) of Fig. 3(a) summarize the wt%-dependent diffracted intensities, band areas, FWHM and crystalline strain for the (002) crystalline phase. As we can see from Fig. 3(a) inset (iii), the largest diffracted intensity and band area occur at 40 wt%. This results in the largest crystalline volume for the increase of wt%. Nevertheless, the 20 wt% sample exhibits the narrowest FWHM (Fig. 3(a) inset (iv)). In principle, a smaller FWHM means a more highly ordered crystalline phase with large crystalline grains and less defects. Moreover, the DebyeIScherrer method was adopted for the analysis of the crystalline strain as it plays an important role for crystal growth and defects. From the observation of Fig. 2 inset (iv), the 20 wt% sample produces the smallest crystalline strain. The samples with the minimum wt% (*i.e.* 10 wt%) contains the largest strain.

The deep explorations for the crystalline orientation and the growth mode of the chiral LHPs was carried out using the grazing-incidence wide-angle X-ray scattering (GIWAXS) technique. The experimental results that are shown in Fig. 3(b)–(f) denote the Bragg diffraction spectra for the (R-MBA)$_2$PbI$_4$ polycrystalline thin films with 20, 40, 10, 30, 60 wt%, respectively. The scattering patterns suggest that all of them have similar crystal structures and components. There are five noticeable features when we compare them: (i) the GIWAXS patterns clearly reveal the side-on crystalline growth mode perpendicular to the substrate along the z-direction for >wt% 10. (ii) In agreement with the XRD spectra, all the GIWAXS patterns give the possible crystalline phases (002l, l = 1, 2, 3, 4, 5). The (002) crystalline phase is still predominant. The change of the wt% such as from 20 wt% to 40 wt% leads to a change in the scattering wavevector from q_z = 0.3 Å^{-1} to 0.39 Å^{-1}, corresponding to the change in the inorganic interlayer distance from 2.1 nm to 1.6 nm. (iii) The one with the 20 wt% possesses considerable polycrystallinity along the in-plane direction (*i.e.* q_{xy}). The scattering pattern exhibits the mostly remarkable arc-shaped feature by comparing with other patterns. (iv) The increase of the wt% from 20 to 40 leads to the shrink of the DebyeoScherrer rings into the individual Bragg spots. (v) The (006), (008) and (0010) crystalline phases become less noticeable for the increase of the wt%.

Based on the SEM, XRD and GIWAXS analyses, the growth mode of the (R-MBA)$_2$PbI$_4$ thin film due to the change of wt% can be understood by the pictorial illustration in Fig. 3(g) and (h). Within a single crystalline grain for (R-MBA)$_2$PbI$_4$, it contains successive lattice planes as shown in Fig. 3(g). The film with 20 wt% has the polycrystalline feature subject to the smooth surface morphology, high crystallinity and relaxed crystalline strain. The crystalline grains are highly ordered in order to fit the crystalline voids and to achieve the smooth surface. Meanwhile, the crystalline strain relaxation can be realized. The increase of the wt% up to 40 or 60 wt% results in relatively rougher surface morphologies, larger crystalline grains and higher crystalline strains. The crystalline voids can be seen as well. In fact, large grain sizes appear to be a limitation for perovskites used for luminescence, while they are more preferable for photovoltaics.[35–38] The growth mode of the chiral LHPs differs from other achiral quasi-2D perovskites

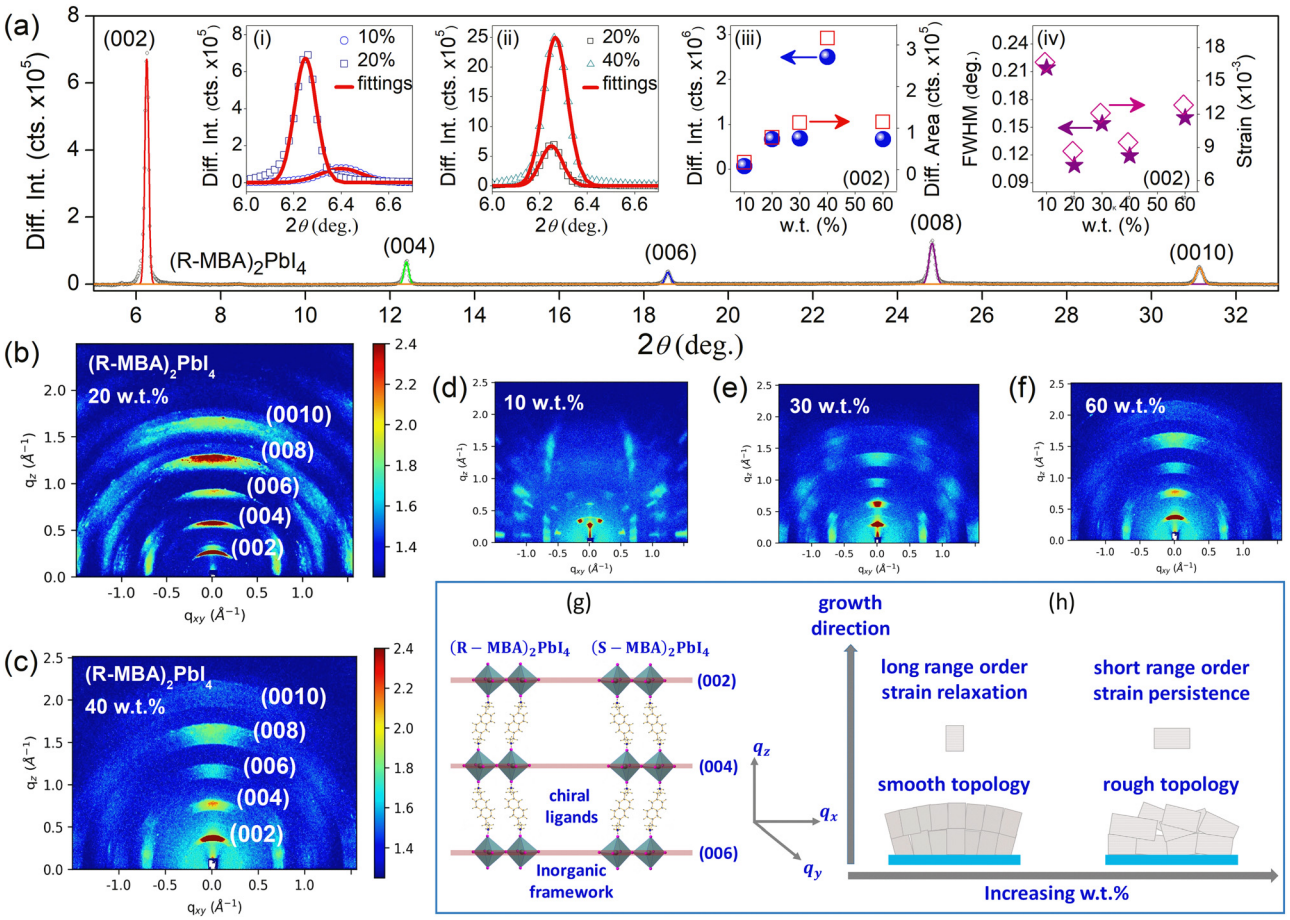

Fig. 3 (a) The XRD spectrum for the (*R*-MBA)$_2$PbI$_4$ polycrystalline film (20 wt%). The red solid lines are the fitting curves. The insets (i and ii) are the zoom-in plots for the (002) diffracted bands of the spectra. (b–f) The GIWAXS patterns for the (*R*-MBA)$_2$PbI$_4$ polycrystalline thin films with 20 wt%, 40 wt%, 10 wt%, 30 wt% and 60 wt%, respectively. (g and h) Pictorial descriptions of the chiral perovskite crystalline structures, out-of-plane orientation and the crystal growth mode. (*R*-MBA)$_2$PbI$_4$ and (*S*-MBA)$_2$PbI$_4$ possess a mirror symmetry.

such as (PEA)$_2$(MA)$_4$Pb$_5$I$_{16}$ (n = 5).[39] In that case, texture growth is more favorable along the (111). By rationally tailoring the wt%, such a growth mode may guarantee the random in-plane distribution of crystalline grains. It helps to reduce the crystalline void, while it gives rise to strain relaxation and a smooth surface.

Despite the discussions about the crystal structure and the growth mechanism, it is of particular significance to link the crystallographic orientations with the NOA for the chiral LHPs. Fig. 4(a)–(e) show the wt%-dependent transmission CD characters for the (*R*-MBA)$_2$PbI$_4$ (red) and (*S*-MBA)$_2$PbI$_4$ (blue) polycrystalline thin films. First, the experimental results verify that chirality can be successfully implemented by chiral organic ligands to an inorganic framework for different wt%. Apparently, the chiral LHPs due to the different wt% have pronounced impact on the CD behavior. The chirality is more conspicuous over a wide range of wavelengths for the 20 wt% sample. By contrast, the spectra do not exhibit identical features. In other words, they do not produce the same transmission symmetry. As we can see from Fig. 4(b), the alternative changes of the CD spectra for $\lambda < 410$ nm originate from different bound exciton transitions.[12] The band-edge transition occurs at approximately 496 nm. When the wt% is equal to 40 and 60 wt% (Fig. 4(d) and (e)), the transmission signals are heavily suppressed for $\lambda < 410$ nm, while the band-edge transition can be still sustained.

In order to further explore the excitonic transition for the chiral LHPs, the wt%-dependent UV-visible photo-absorption spectra within the same measuring range are examined and the results are given in Fig. 4(f)–(j) for (*R*-MBA)$_2$PbI$_4$. The same absorption spectrum can be obtained for (*S*-MBA)$_2$PbI$_4$. From the observation of the spectra, they all have the absorption band edges at approximately λ = 496 nm. Such absorption is primarily ascribed to the delocalized and less bound Wannier excitons for the quasi-2D perovskites with $n \geq 2$ (n denotes the number of perovskite sublattices).[33] However, it should be noted that two distinguished absorption bands at λ = 338 nm and 371 nm can be well resolved for the 20 wt% sample. They tend to become less noticeable for the increase of the wt%. These two photo-absorption bands are indeed attributed to the existence of photogenerated bound excitons for the reduced-dimensional RP-type chiral perovskites, such as n = 1, 2. These

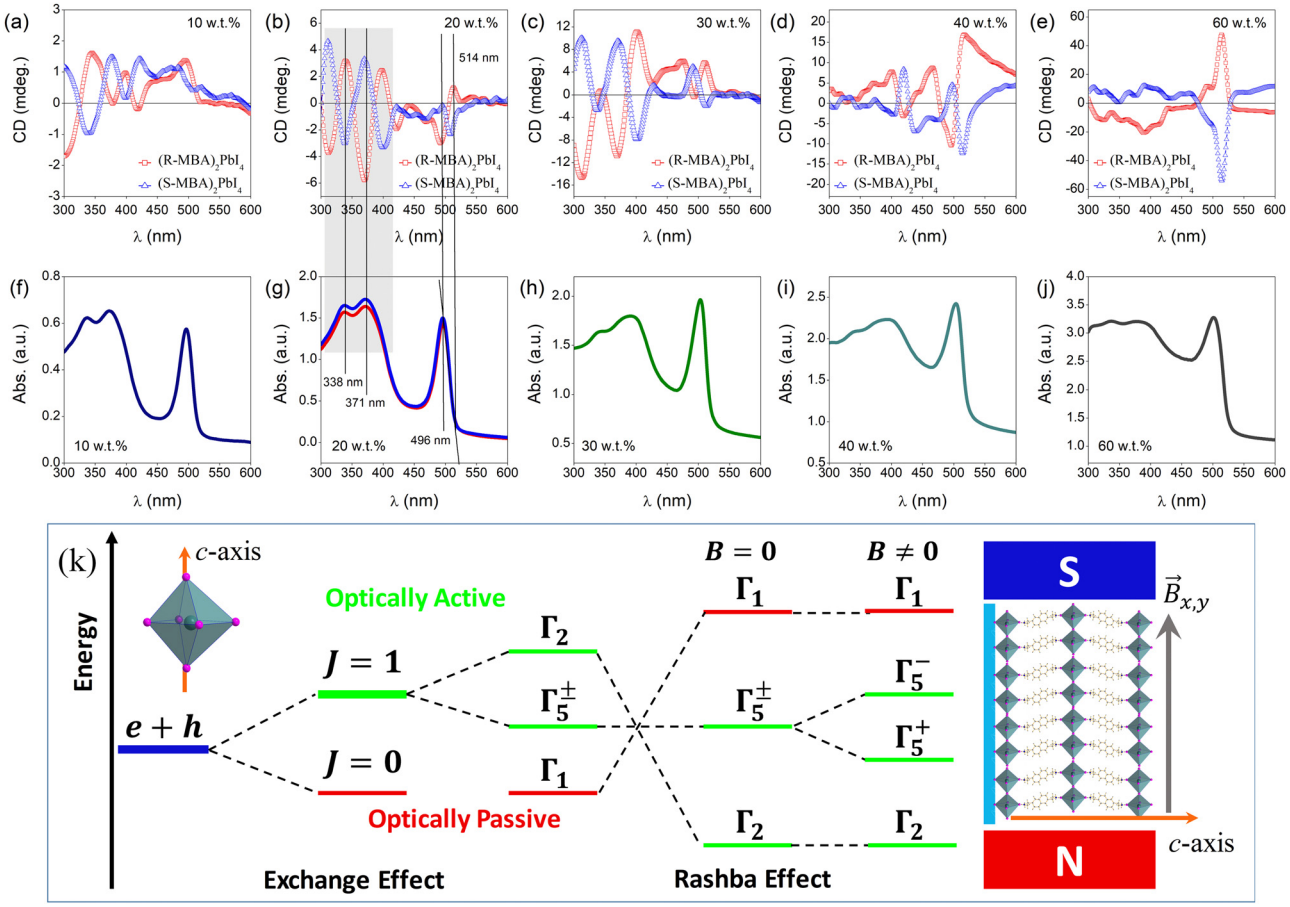

Fig. 4 (a–e) Plots of wt% (*i.e.*, 10%, 20%, 30%, 40% and 60%)-dependent CD transmission spectra for the (*R*-MBA)$_2$PbI$_4$ and (*S*-MBA)$_2$PbI$_4$ thin films. (f–j) The corresponding UV-visible photo-absorption spectra. All the spectra were recorded under the ambient condition. (k) Schematic illustration for the exciton fine structure in a lead halide perovskite. The electron–hole (e + h) exchange effect splits the fourfold degenerate lowest energies of the exciton in a triplet (bright states) and a singlet (dark state). *J* denotes the total angular momentum. Γ_1, Γ_2, and $\Gamma_5^{\pm}$ are explained in the main content.

absorption bands gradually diminish with the increase of wt%, indicating the suppression of the exciton transitions. The results are consistent with the CD spectra of Fig. 4 and the wt%-dependent PL intensity shown in Fig. 1(e). All the spectroscopic characterizations reveal that the increase of wt% leads to the reduction of the exciton transitions. Since the transitions decides the magnitude of the magneto-PL, the effect is reduced for the large wt%.

Based on the aforesaid crystallographic and optical characterizations for the chiral LHPs, we consider that the wt% dependence of magneto-PL has a close relationship to the crystallographic orientation and chiral-induced exciton transitions. As we know, the chiral LHPs contain the octahedral lead halide inorganic framework, integrated with the enantiomeric organic interlayer. They have the pure 2-fold screw symmetry so that they belong to a chiral space group ($P2_12_12_1$),[40] whereas the electronic and magnetic structures are primarily decided by the inorganic framework, and consequently it determines optical transitions.[41] The chiral organic ligands offer possibility for the CD behavior. The field-induced Zeeman splitting and energy level mixing at excited states can further make multiple transitions such as the circularly polarized light emissions. In fact, the splitting and mixing can be effectively triggered by the magnetic field along the *c*-axis of the octahedral crystal.[18,21] Fig. 4(k) provides the sketch for the comprehensive understanding of the magneto-PL. Because of the electron–hole exchange effect, the quantum exciton has the total angular momentum of $J = 0$ or 1, depending on their spin antiparallel and parallel configurations. They are also known to achieve dark and bright states at excitonic states.[42–44] There are indeed four quantum exciton states, including Γ_1 (dark), Γ_2 (linear polarized emission along the *z*-axis), and $\Gamma_5^{\pm}$ (doubly degenerate, left and right circularly polarized emission along two perpendicular in-plane *x* and *y* axis).[18] The four exciton states can be written as:[18,41]

$$|\Gamma_1\rangle = \frac{1}{\sqrt{2}}(|c_+\bar{v}_-\rangle - |c_-\bar{v}_+\rangle),$$
$$|\Gamma_2\rangle = \frac{1}{\sqrt{2}}(|c_+\bar{v}_-\rangle + |c_-\bar{v}_+\rangle), \quad (1)$$
$$|\Gamma_5^{\pm}\rangle = |c_\pm\bar{v}_\pm\rangle,$$

where $c_\pm$ and $\bar{v}_\pm$ are used to denote the electron and hole states, respectively. The subscripts $\pm$ represent the spin-up ($\uparrow$) and

-down (↓) components. An exciton may have one of the four possible spin configurations such as $c_+\bar{v}_+$, $c_-\bar{v}_-$, $c_+\bar{v}_-$ and $c_-\bar{v}_+$. The CISOC can interfere with the four exciton states leading to two indirect parabolic bands in the momentum space. We mainly consider the $\Gamma_5^{\pm}$ values since they are associated with the CPL. Even without magnetic fields, the existence of the Rashba effect that stems from the crystalline structural inversion asymmetry may adjust the relative positions of the energy levels for the bright and dark states.[42] When an in-plane magnetic field ($B_{x,y}$) is applied, it helps to mix $\Gamma_5^{\pm}$ and Γ_2 to a certain extent due to the Zeeman effect. Upon mixing, the circularly polarized photoluminescence intensity is decided by the oscillation strength difference (*i.e.* O_2–O_5), and the generation rate difference (*i.e.* F_2–F_5) of the two states (*i.e.* Γ_2 and $\Gamma_5^{\pm}$).[18] For the given chiral LHPs with opposite helicity ($\tau = \pm 1$), the mixing strengths should be converse for $\Gamma_2 + \Gamma_5^+$ and $\Gamma_2 + \Gamma_5^-$ (Fig. S5, ESI†). Thus, magneto-PL is determined simultaneously by the Rashba induced excitonic states and CISOC, while the applied magnetic field is responsible for generating the Zeeman effect for mixing. Based on the observation of the GIWAXS spectra shown in Fig. 3, we have found that the in-plane crystallographic orientation can be affected by changing the wt% for the precursor solutions. Depending on the alignment for the in-plane $B_{x,y}$ with respect to the crystalline *c*-axis of the chiral LHPs, the Zeeman splitting and the mixing strengths can be different for the films fabricated with the distinct wt%. The magnitude of the magneto-PL can be altered. In addition to the magnetic field, the exciton transitions are also decided by electric field vectors ($E_{x,y}$) with respect to the crystalline phases of the 2D layered perovskite. When the $E_{x,y}$ is perpendicular to the *c*-axis of the chiral LHPs for the (002) crystalline growth mode, the optical transition to the exciton state exhibits the $\Gamma_5^{\pm}$ symmetry. One the other hand, the Γ_2 symmetry is allowed for the $E_{x,y}$ in parallel with the *c*-axis.[12,45] This also explains that the exciton transitions-related CD spectra can vary due to the crystalline orientation.

4. Summary

In the work, we conducted a systematic study on the impact of crystallographic orientations on the chiral-induced magneto-PL and the CD character. By simply tuning the wt% of precursor solutions, the large magneto-PL effect with strong tunability could be realized. The effect relies on the field-modulated electronic fine structures for the exciton states. We postulate that diploe-allowed excitonic transitions and CD characters can be dramatically influenced by the crystalline orientation. The complete understanding of the crystalline growth mode and the chiroptical property is of critical importance for achieving the large magneto-PL with strong tunability. Our work paves the way for future perovskite spin-chiroptical applications.

Data availability statement

The data that support the finding of the study are available from the corresponding author upon reasonable request.

Conflicts of interest

The authors declare no conflict of interest.

Acknowledgements

The work was supported by the Fundamental Research Funds for the Central Universities (2021YJS177), the National Natural Science Foundation of China (Grant No. 61634001), and the Intergovernmental Cooperation Project, National Key Research and Development Program, Ministry of Science and Technology, China (Grant No. 2019YFE0108400).

References

1 J. Calabrese, N. L. Jones, R. L. Harlow, N. Herron, D. L. Thorn and Y. Wang, *J. Am. Chem. Soc.*, 1991, **113**, 2328–2330.
2 G. Pacchioni, *Nat. Rev. Mater.*, 2021, **6**, 108.
3 W. Xu, Q. Hu, S. Bai, C. Bao, Y. Miao, Z. Yuan, T. Borzda, A. J. Barker, E. Tyukalova, Z. Hu, M. Kawecki, H. Wang, Z. Yan, X. Liu, X. Shi, K. Uvdal, M. Fahlman, W. Zhang, M. Duchamp, J.-M. Liu, A. Petrozza, J. Wang, L.-M. Liu, W. Huang and F. Gao, *Nat. Photonics*, 2019, **13**, 418–424.
4 X.-K. Liu, W. Xu, S. Bai, Y. Jin, J. Wang, R. H. Friend and F. Gao, *Nat. Mater.*, 2021, **20**, 10–21.
5 X. Sun, C. Han, K. Wang, H. Yu, J. Li, K. Lu, J. Qin, H. Yang, L. Deng, F. Zhao, Q. Yang and B. Hu, *ACS Appl. Energy Mater.*, 2018, **1**, 6992–6998.
6 L. Mao, C. C. Stoumpos and M. G. Kanatzidis, *J. Am. Chem. Soc.*, 2019, **141**, 1171–1190.
7 X. Sun, C. Han, Z. Liu, L. Xu, J. Li, H. Yu and K. Wang, *J. Phys. Chem. C*, 2020, **124**, 28417–28423.
8 P. Liu, S. Yu and S. Xiao, *Sustainable Energy Fuels*, 2021, **5**, 3950–3978.
9 D. Thrithamarassery Gangadharan and D. Ma, *Energy Environ. Sci.*, 2019, **12**, 2860–2889.
10 G. K. Long, R. Sabatini, M. I. Saidaminov, G. Lakhwani, A. Rasmita, X. G. Liu, E. H. Sargent and W. B. Gao, *Nat. Rev. Mater.*, 2020, **5**, 423–439.
11 Y. Dang, X. Liu, B. Cao and X. Tao, *Matter*, 2021, **4**, 794–820.
12 J. Ahn, E. Lee, J. Tan, W. Yang, B. Kim and J. Moon, *Mater. Horiz.*, 2017, **4**, 851–856.
13 H. P. Lu, J. Y. Wang, C. X. Xiao, X. Pan, X. H. Chen, R. Brunecky, J. J. Berry, K. Zhu, M. C. Beard and Z. V. Vardeny, *Sci. Adv.*, 2019, **5**, eaay0571.
14 C. Yuan, X. Li, S. Semin, Y. Feng, T. Rasing and J. Xu, *Nano Lett.*, 2018, **18**, 5411–5417.
15 C. K. Yang, W. N. Chen, Y. T. Ding, J. Wang, Y. Rao, W. Q. Liao, Y. Y. Tang, P. F. Li, Z. X. Wang and R. G. Xiong, *Adv. Mater.*, 2019, **31**, e1808088.
16 R. G. Xiong, S. Q. Lu, Z. X. Zhang, H. Cheng, P. F. Li and W. Q. Liao, *Angew. Chem., Int. Ed.*, 2020, **59**, 9574–9578.
17 C. Yuan, X. Li, S. Semin, Y. Feng, T. Rasing and J. Xu, *Nano Lett.*, 2018, **18**, 5411–5417.
18 R. Pan, K. Wang and Z.-G. Yu, *Mater. Horiz.*, 2022, **9**, 740–747.

19 Z. J. Huang, B. P. Bloom, X. J. Ni, Z. N. Georgieva, M. Marciesky, E. Vetter, F. Liu, D. H. Waldeck and D. L. Sun, *ACS Nano*, 2020, **14**, 10370–10375.
20 R. Pan, S. Tao, L. Kan, J. Hu, J. Li, Y. Li, X. Zhang and K. Wang, *Adv. Opt. Mater.*, 2022, **10**, 2200064.
21 Z. G. Yu, *J. Phys. Chem. Lett.*, 2020, **11**, 8638–8646.
22 Y.-H. Kim, Y. Zhai, H. Lu, X. Pan, C. Xiao, E. A. Gaulding, S. P. Harvey, J. J. Berry, Z. V. Vardeny, J. M. Luther and M. C. Beard, *Science*, 2021, **371**, 1129–1133.
23 S.-H. Yang, R. Naaman, Y. Paltiel and S. S. P. Parkin, *Nat. Rev. Phys.*, 2021, **3**, 328–343.
24 D. Liang, C. Dong, L. Cai, Z. Su, J. Zang, C. Wang, X. Wang, Y. Zou, Y. Li, L. Chen, L. Zhang, Z. Hong, A. El-Shaer, Z.-K. Wang, X. Gao and B. Sun, *Small*, 2021, **17**, 2100972.
25 K. Meng, X. Wang, Q. Xu, Z. Li, Z. Liu, L. Wu, Y. Hu, N. Liu and G. Chen, *Adv. Funct. Mater.*, 2019, **29**, 1902319.
26 K. Wang, C. Wu, D. Yang, Y. Jiang and S. Priya, *ACS Nano*, 2018, **12**, 4919–4929.
27 S. Ma, Y.-K. Jung, J. Ahn, J. Kyhm, J. Tan, H. Lee, G. Jang, C. U. Lee, A. Walsh and J. Moon, *Nat. Commun.*, 2022, **13**, 3259.
28 X. Yang, X. Zhang, J. Deng, Z. Chu, Q. Jiang, J. Meng, P. Wang, L. Zhang, Z. Yin and J. You, *Nat. Commun.*, 2018, **9**, 570.
29 L. Kong, X. Zhang, Y. Li, H. Wang, Y. Jiang, S. Wang, M. You, C. Zhang, T. Zhang, S. V. Kershaw, W. Zheng, Y. Yang, Q. Lin, M. Yuan, A. L. Rogach and X. Yang, *Nat. Commun.*, 2021, **12**, 1246.
30 Y. Han, S. Park, C. Kim, M. Lee and I. Hwang, *Nanoscale*, 2019, **11**, 3546–3556.
31 A. a O. El-Ballouli, O. M. Bakr and O. F. Mohammed, *J. Phys. Chem. Lett.*, 2020, **11**, 5705–5718.
32 R. Chakraborty, G. Paul and A. J. Pal, *Phys. Rev. Appl.*, 2022, **17**, 054045.
33 G. Long, C. Jiang, R. Sabatini, Z. Yang, M. Wei, L. N. Quan, Q. Liang, A. Rasmita, M. Askerka, G. Walters, X. Gong, J. Xing, X. Wen, R. Quintero-Bermudez, H. Yuan, G. Xing, X. R. Wang, D. Song, O. Voznyy, M. Zhang, S. Hoogland, W. Gao, Q. Xiong and E. H. Sargent, *Nat. Photonics*, 2018, **12**, 528–533.
34 L. N. Quan, Y. Zhao, F. P. García de Arquer, R. Sabatini, G. Walters, O. Voznyy, R. Comin, Y. Li, J. Z. Fan, H. Tan, J. Pan, M. Yuan, O. M. Bakr, Z. Lu, D. H. Kim and E. H. Sargent, *Nano Lett.*, 2017, **17**, 3701–3709.
35 W. Nie, H. Tsai, R. Asadpour, J.-C. Blancon, A. J. Neukirch, G. Gupta, J. J. Crochet, M. Chhowalla, S. Tretiak, M. A. Alam, H.-L. Wang and A. D. Mohite, *Science*, 2015, **347**, 522–525.
36 S. Wang, Z. Ma, B. Liu, W. Wu, Y. Zhu, R. Ma and C. Wang, *Sol. RRL*, 2018, **2**, 1800034.
37 X. Xu, Y. Sun, D. He, Z. Liang, G. Liu, S. Xu, Z. Li, L. Zhu and X. Pan, *J. Mater. Chem. C*, 2021, **9**, 208–213.
38 G. Jia, Z.-J. Shi, Y.-D. Xia, Q. Wei, Y.-H. Chen, G.-C. Xing and W. Huang, *Opt. Express*, 2018, **26**, A66–A74.
39 F. Huang, P. Siffalovic, B. Li, S. Yang, L. Zhang, P. Nadazdy, G. Cao and J. Tian, *Chem. Eng. J.*, 2020, **394**, 124959.
40 P. S. Halasyamani and K. R. Poeppelmeier, *Chem. Mater.*, 1998, **10**, 2753–2769.
41 Z. G. Yu, *Sci. Rep.*, 2016, **6**, 28576.
42 A. Meijerink and F. T. Rabouw, *Nat. Mater.*, 2019, **18**, 660–661.
43 M. A. Becker, R. Vaxenburg, G. Nedelcu, P. C. Sercel, A. Shabaev, M. J. Mehl, J. G. Michopoulos, S. G. Lambrakos, N. Bernstein, J. L. Lyons, T. Stöferle, R. F. Mahrt, M. V. Kovalenko, D. J. Norris, G. Rainò and A. L. Efros, *Nature*, 2018, **553**, 189–193.
44 P. Tamarat, M. I. Bodnarchuk, J.-B. Trebbia, R. Erni, M. V. Kovalenko, J. Even and B. Lounis, *Nat. Mater.*, 2019, **18**, 717–724.
45 K. Tanaka, T. Takahashi, T. Kondo, K. Umeda, K. Ema, T. Umebayashi, K. Asai, K. Uchida and N. Miura, *Jpn. J. Appl. Phys.*, 2005, **44**, 5923–5932.